ADVANCED ENERGY MATERIALS
www.advenergymat.de

Optimizing Li-Excess Cation-Disordered Rocksalt Cathode Design Through Partial Li Deficiency

*Liliang Huang, Peichen Zhong, Yang Ha, Zijian Cai, Young-Woon Byeon, Tzu-Yang Huang, Yingzhi Sun, Fengyu Xie, Han-Ming Hau, Haegyeom Kim, Mahalingam Balasubramanian, Bryan D. McCloskey, Wanli Yang, and Gerbrand Ceder**

Li-excess disordered rocksalts (DRXs) are emerging as promising cathode materials for Li-ion batteries due to their ability to use earth-abundant transition metals. In this work, a new strategy based on partial Li deficiency engineering is introduced to optimize the overall electrochemical performance of DRX cathodes. Specifically, by using Mn-based DRX as a proof-of-concept, it is demonstrated that the introduction of cation vacancies during synthesis (e.g., $Li_{1.3-x}Mn^{2+}_{0.4-x}Mn^{3+}_{x}Nb_{0.3}O_{1.6}F_{0.4}$, $x = 0$, 0.2, and 0.4) improves both the discharge capacity and rate performance due to the more favored short-range order in the presence of Mn^{3+}. Density functional theory calculations and Monte Carlo simulations, in combination with spectroscopic tools, reveal that introducing 10% vacancies ($Li_{1.1}Mn^{2+}_{0.2}Mn^{3+}_{0.2}Nb_{0.3}O_{1.6}F_{0.4}$) enables both Mn^{2+}/Mn^{3+} redox and excellent Li percolation. However, a more aggressive vacancy doping (e.g., 20% vacancies in $Li_{0.9}Mn^{3+}_{0.4}Nb_{0.3}O_{1.6}F_{0.4}$) impairs performance because it induces phase separation between an Mn-rich and a Li-rich phase.

1. Introduction

The market for Li-ion batteries has witnessed tremendous growth over the past decades.[1–4] Society's transition towards carbon neutrality[5] creates urgency for the development of novel cathode materials, as the cost and metal use of current cathode materials limits very large-scale application of Li-ion batteries.[2–4,6] The recent development of Li-excess cation-disordered rocksalt (DRX) cathodes greatly expands the chemical design space for designing high-performance cathodes, creating opportunities for the use of earth-abundant metals.[7–13] To date, DRX cathodes with capacities as high as 300 mAh g^{-1} have been made with many transition-metal elements (e.g., Mn, Ti, V, and Cr),[9–11,14–16] some of which have recently shown excellent rate performance (e.g., $Li_{1.2}Mn_{0.2}Cr_{0.2}Ti_{0.4}O_2$ and $Li_{1.3}Mn_{0.2}Co_{0.1}Cr_{0.1}Ti_{0.1}Nb_{0.2}O_{1.7}F_{0.3}$).[11,16] Because of the lack of long-range cation ordering, DRX compounds exhibit simple rocksalt diffraction patterns, hiding the underlying complexity of the local cation short-range ordering (SRO, or short-range correlation) which has been shown to strongly affect their capacity and rate performance.[10,11,13,17–21] The strong correlation between cation SRO and performance is the result of the unique Li-diffusion mechanism in DRX: Because of the small lattice parameters of these rocksalts, Li^+ can only diffuse between two octahedral sites through an activated tetrahedral site with no face-sharing TM cations, termed a 0-TM channel.[12,22,23] To realize bulk-scale Li transport, a percolating 0-TM network is required throughout the structure. Percolation is controlled by the amount of 0-TM environments and their arrangement, both of which are influenced by the cation SRO.[10,11,13,18] Unlike in ordered compounds, where long-range cation ordering determines the local environment, remarkable variations in local environments can exist within DRX, influenced by composition,[13] annealing time,[24] and

L. Huang, P. Zhong, Z. Cai, Y.-W. Byeon, Y. Sun, F. Xie, H.-M. Hau, H. Kim, G. Ceder
Materials Sciences Division
Lawrence Berkeley National Laboratory
Berkeley, CA 94720, USA
E-mail: gceder@berkeley.edu

P. Zhong, Z. Cai, Y. Sun, F. Xie, H.-M. Hau, G. Ceder
Department of Materials Science and Engineering
University of California Berkeley
Berkeley, CA 94720, USA

The ORCID identification number(s) for the author(s) of this article can be found under https://doi.org/10.1002/aenm.202202345.

DOI: 10.1002/aenm.202202345

Y. Ha, W. Yang
Advanced Light Source
Lawrence Berkeley National Laboratory
Berkeley, CA 94720, USA

T.-Y. Huang, B. D. McCloskey
Department of Chemical and Biomolecular Engineering
University of California Berkeley
Berkeley, CA 94720, USA

T.-Y. Huang, B. D. McCloskey
Energy Storage and Distributed Resources Division
Lawrence Berkeley National Laboratory
Berkeley, CA 94720, USA

M. Balasubramanian
Advanced Photon Source–X-ray Science Division
Argonne National Laboratory
Argonne, IL 60439, USA

even the number of metal cations present.[11] Such cation SRO in DRX is in part controlled by charge balance (high-valent TMs tend to mix with Li^+ to maintain local electroneutrality, thereby reducing 0-TM formation), and by the difference in ionic radius (the size mismatch between Li^+ and TM cations facilitates Li segregation to minimize strain, thus promoting 0-TM formation).[13] Multiple approaches to influence SRO have been reported in the literature, such as the selection of redox-inactive TM elements[13] and high-entropy systems.[11] In this paper, using Mn-based DRX as a proof-of-concept, we show that SRO of materials that are nominally the same can also be simply controlled by introducing Li deficiency during synthesis. This novel approach can therefore be used to enhance the capacity and rate performance of a DRX without the need to change to the transition metal content.

The low cost and abundance of Mn, and the good thermal stability of the Mn^{4+} charged state make Mn-based DRX promising cathode materials[10,18] A general dilemma researchers face while designing Mn-based DRX is the choice of Mn^{2+} or Mn^{3+} in the as-synthesized state. From a theoretical TM capacity perspective Mn^{2+} is favored over Mn^{3+} as it delivers double electron redox, mitigating the reliance on oxygen redox.[9,18] However, Mn^{2+} is closer in size to Li^+ than Mn^{3+} and tends to mix more with Li^+ which reduces the amount of 0-TM channels implying lower rate performance. To address this issue, it would be favorable to synthesize DRX with Mn^{3+} to obtain good rate performance, but still be able to use Mn^{2+}/Mn^{3+} redox to achieve high capacity. Herein, we demonstrate that this can be realized by synthesizing the material in a partially delithiated state, where the vacancy sites in the as-synthesized Mn^{3+}-based DRX will be refilled with Li^+ after the initial discharge process. Specifically, we experimentally and computationally investigate a series of Mn-Nb-based DRX ($Li_{1.3-x}Mn^{2+}_{0.4-x}Mn^{3+}_{x}Nb_{0.3}O_{1.6}F_{0.4}$, $x = 0$, 0.2, and 0.4). While Nb should not be considered earth-abundant, to demonstrate proof-of-concept the use a higher valent stabilizer like Nb^{5+} is advantageous because it allows for using a higher Li-excess level and thus a wider range of cation vacancy concentrations. However, the concept demonstrated in this paper should remain applicable to Mn-Ti based DRX systems, which contain only abundant transition metals. We find that the substitution of Mn^{2+} by Mn^{3+} by incorporating cation vacancies improves both the discharge capacity and rate performance. Using density functional theory (DFT)-based calculations, we elucidate how the introduction of cation vacancies affects the cation SRO and phase stability of the DRX structure. We show that to fully utilize the beneficial effect of cation vacancies on percolation properties, their concentration needs to be properly controlled without destroying the DRX structure (e.g., optimal performance is achieved for $Li_{1.1}Mn^{2+}_{0.2}Mn^{3+}_{0.2}Nb_{0.3}O_{1.6}F_{0.4}$ with 10% cation vacancies). This composition has half of the Mn in the +3 state to improve the as-synthesized SRO, but can discharge all Mn to the Mn^{2+} state.

2. Results

2.1. Structural characterization

A mechanochemical ball-milling method[9,10] was employed to synthesize cation-disordered $Li_{1.3}Mn^{2+}_{0.4}Nb_{0.3}O_{1.6}F_{0.4}$ (L13MNOF), $Li_{1.1}Mn^{2+}_{0.2}Mn^{3+}_{0.2}Nb_{0.3}O_{1.6}F_{0.4}$ (L11MNOF), and $Li_{0.9}Mn^{3+}_{0.4}Nb_{0.3}O_{1.6}F_{0.4}$ (L09MNOF) (**Figure 1** and Table S1, Supporting Information). The X-ray diffraction (XRD) patterns of L13MNOF and L11MNOF compounds can be indexed to a DRX structure without obvious impurity peaks (Figure 1A and Table S2, Supporting Information). The Rietveld refinement results indicate that L13MNOF has a larger lattice parameter (4.2261 Å) than L11MNOF (4.2110 Å), consistent with the larger ionic radius of Mn^{2+} (0.83 Å) than Mn^{3+} (0.65 Å).[25] For L09MNOF, several Mn_2O_3 peaks appeared in the XRD pattern in addition to the DRX phase. Therefore, we included Mn_2O_3 as an impurity phase in the refinement for L09MNOF, in addition to a simple rocksalt structural model. The compound was refined to contain 4.5% Mn_2O_3 and 95.5% DRX phase. The formation of a single-phase DRX structure for L11MNOF and L13MNOF was further confirmed by electron diffraction (Figure 1C,F). Due to the small crystallite size of these ball-mill-synthesized samples, only diffraction rings are observed. This is in contrast to the diffraction patterns from solid-state-synthesized DRX samples, which can exhibit Bragg diffraction spots and diffuse scattering patterns (induced by the cation SRO).[11,13] The scanning transmission electron microscopy (STEM) images and corresponding energy-dispersive X-ray spectroscopy (EDS) elemental maps (Figure 1D,G, and Figure S1, Supporting Information) reveal that the component elements (Mn, Nb, O, and F) are uniformly distributed within L13MNOF and L11MNOF nanoparticles while distinct Mn- and O-rich regions exist in the L09MNOF nanoparticle, consistent with the observation from XRD that an impurity Mn_2O_3 phase forms in L09MNOF. In addition to the crystal structure, the nanoparticle size and morphology can also greatly affect the cathode performance.[26–30] As such, we collected scanning electron microscopy (SEM) images (Figure 1B,E, and Figure S2, Supporting Information) for these compounds and confirmed that all of them have a similar quasi-spherical shape with primary particle sizes ranging from 100 to 200 nm.

2.2. Electrochemical Performance

The electrochemical performance of the Li–Mn—Nb—O–F compounds were tested in galvanostatic mode at room temperature (**Figure 2**). The open circuit voltages of the as-synthesized samples increase in the order of L13MNOF < L11MNOF < L09MNOF, consistent with the increased Mn valences (Figure 2A–C). When cycled between 1.5 and 5 V at a current density of 20 mA g^{-1}, the first-cycle charge capacity decreased in the order of L13MNOF (334 mAh g^{-1}) > L11MNOF (280 mAh g^{-1}) > L09MNOF (218 mAh g^{-1}) (Figure 2A–C), consistent with their decreasing theoretical Li capacities. Interestingly, upon discharge, L13MNOF delivered the lowest capacity among the three compounds: 258 mAh g^{-1} (810 Wh kg^{-1}) for L13MNOF, 283 mAh g^{-1} (885 Wh kg^{-1}) for L11MNOF, and 272 mAh g^{-1} (832 Wh kg^{-1}) for L09MNOF (Figure 2A–C and Table S3, Supporting Information). The galvanostatic intermittent titration measurements (Figure S3, Supporting Information) show that L11MNOF and L09MNOF exhibit significantly smaller overpotentials than L13MNOF during the discharge process, indicating improved kinetics in these

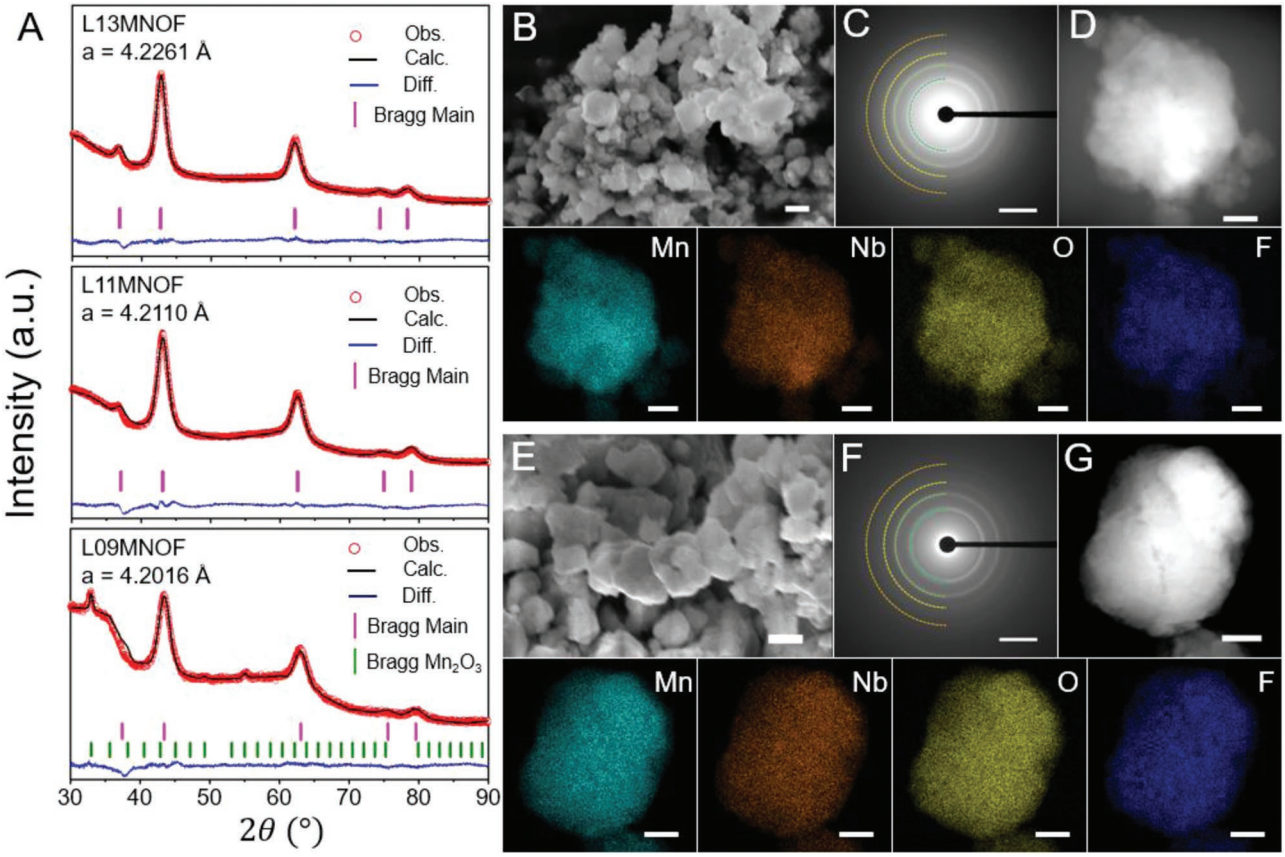

Figure 1. A) XRD patterns and refinement results for L13MNOF, L11MNOF, and L09MNOF, where *a* is the refined lattice constant, and the Bragg positions are indicated by vertical magenta and olive bars. Obs., Calc., Diff. represent the observed pattern, calculated pattern, and the difference between the observed and calculated patterns, respectively. B) SEM image, C) electron diffraction pattern, and D) STEM image and corresponding EDS elemental maps for L13MNOF. E) SEM image, F) electron diffraction pattern, and G) STEM image and corresponding EDS elemental maps for L11MNOF. The electron diffraction patterns in (C) and (F) can be indexed to a DRX phase, with the *d* spacings determined to be 2.1, 1.5, 1.2, and 0.9 Å. Scale bars: 200 nm in (B) and (E), 5 nm^{-1} in (C) and (F), and 50 nm in (D) and (G).

two compounds. The effect of cation vacancies on improved Li transport is further corroborated by the superior rate performance of L11MNOF and L09MNOF (Figure 2D–F). For example, upon increasing the current density from 20 to 1000 mA g^{-1}, the discharge capacity for L13MNOF decreased from 258 to 113 mAh g^{-1}, corresponding to a 56.2% capacity loss at the high rate. In contrast, the capacity loss was reduced to 50.4% for L09MNOF and to 43.1% for L11MNOF, and a large discharge capacity of 161 mAh g^{-1} continued to be delivered at 1000 mA g^{-1} for L11MNOF. Note that these three compounds can be essentially regarded as three different states of a single material under a topotactic transformation, which in principle would not give rise to observable differences in overall performance. Therefore, the electrochemical test results strongly suggest that the introduction of cation vacancies during the synthesis modifies the local chemical ordering within the compound, which improves its percolation properties. To obtain a better understanding of the relationship among composition, chemical ordering, and electrochemical performance, we further systemically explored the redox mechanisms and local SRO in these compounds, the results of which are discussed in the following sections.

2.3. Redox Mechanism

Li-ion intercalation/deintercalation is locally charge balanced by redox reactions of the transition-metal cations and oxygen anions. Here, the redox mechanism in L13MNOF, L11MNOF, and L09MNOF compounds was examined by combining ex situ hard X-ray absorption spectroscopy (XAS) and soft X-ray mapping of resonant inelastic X-ray scattering (mRIXS) at selected states of charge and discharge in the first electrochemical cycle. The Mn K-edge X-ray near-edge structure (XANES) results (**Figure 3**A-C) suggest that for the pristine samples, the Mn K-edge energy increases in the order of L13MNOF < L11MNOF < L09MNOF, consistent with their predesigned increasing Mn valence states (+2 for L13MNOF, +2.5 for L11MNOF, and +3 for L09MNOF). Moreover, Mn^{2+}/Mn^{4+} double electron redox is (partially) available in L13MNOF (Figure 3A). Specifically, as the charge capacity increases from 0 to 120 mAh g^{-1} and then to top of charge (5 V), the Mn K-edge shifts from an energy close to MnO (Mn^{2+} reference) to that of Mn_2O_3 (Mn^{3+} reference) and then approaches that of MnO_2 (Mn^{4+} reference). Similar Mn oxidation leading to Mn^{4+} at the top of charge is also observed in L11MNOF and L09MNOF (Figure 3B,C). Upon discharging

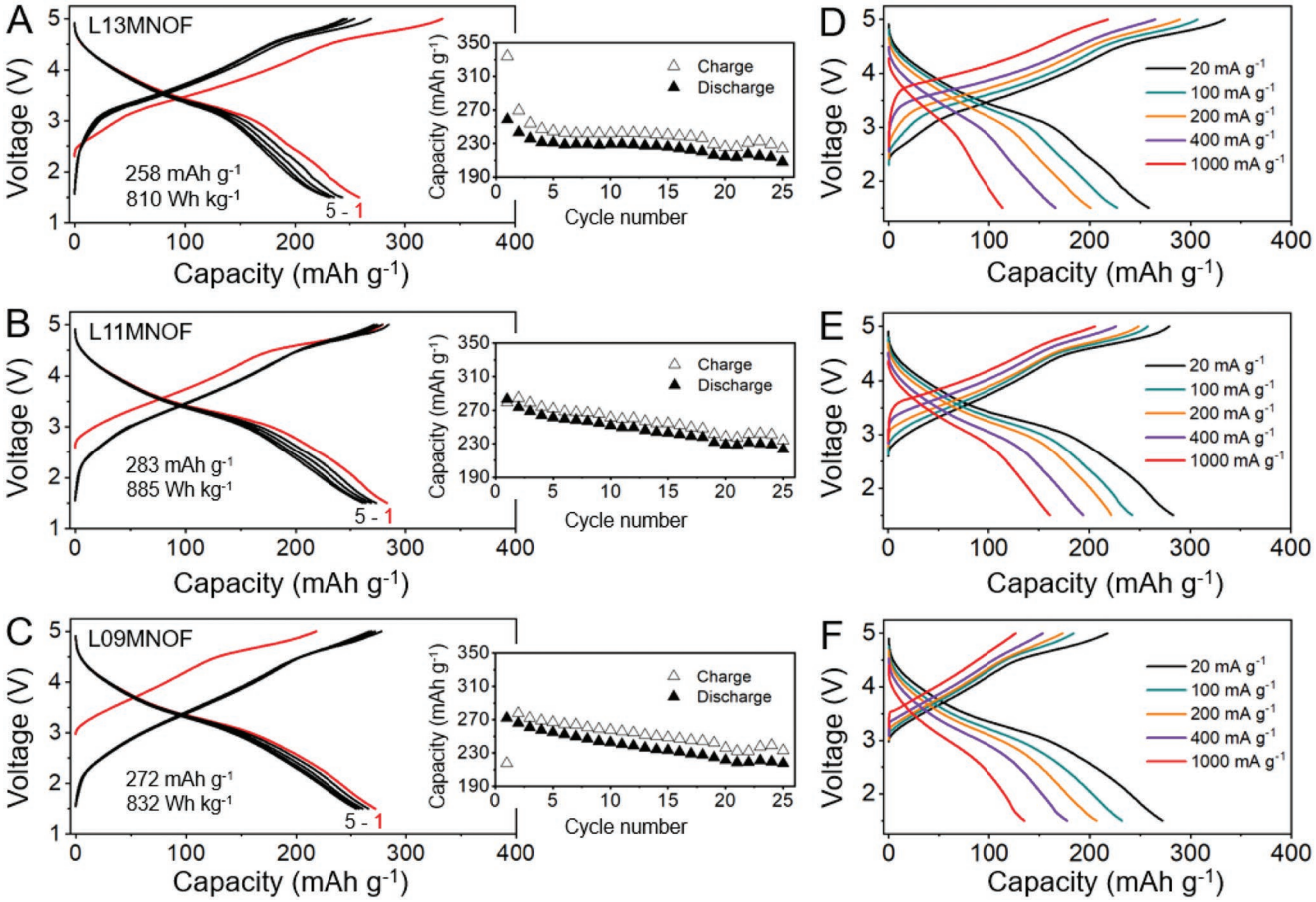

Figure 2. Voltage profiles of A) L13MNOF, B) L11MNOF, and C) L09MNOF within the voltage window of 1.5–5 V at 20 mA g^{-1} and room temperature. The voltage profiles of cycle 1 are plotted in red, and the rest are plotted in black. The corresponding capacity-retention plots for each compound over 25 cycles are shown as insets. First-cycle voltage profiles of D) L13MNOF, E) L11MNOF, and F) L09MNOF at different current densities.

to 1.5 V, the XANES spectra of all three compounds return to an energy close to that of MnO, indicating the excellent reversibility of the Mn redox. The Nb K-edge shows little shift in all three samples, indicating that Nb^{5+} is not redox-active within the applied voltage window (Figure S4, Supporting Information), consistent with previous literature results.[9,11]

Because the main edge of the XANES spectra corresponds to dipole excitation from 1*s* to 4*p* states instead of to the 3*d* valence state, the technique is not ideal for precise quantification of Mn oxidation states.[31] We therefore further quantify the evolution of Mn valence states as a function of the state of charge and discharge using the Mn L_3-edge spectra derived from the mRIXS inverse partial fluorescence yield (iPFY) signal. As shown in Figure 3D,E and Figure S5, Supporting Information, at the top of charge, the Mn valence state in all three samples is ≈+3.6 rather than +4. Such incomplete oxidation has also been observed in other Li–Mn—O–F systems synthesized via a similar mechanochemical ball-milling method.[9,10] It has been shown that both the large lattice constant and the presence of Mn–F bonds can modify the overlap between Mn and O redox, which prevents Mn from being fully oxidized to Mn^{4+}.[9,10] Upon discharge, the valence state of Mn decreases to approximately +2.1 in all three samples, consistent with the XANES results. These results indicate that in these compounds, the Mn-reduction process only contributes ≈0.6 e^- per formula unit (*f.u.*) during discharge, which is smaller than the experimentally realized capacities (e.g., 0.89 e^- per *f.u.* for L13MNOF and 0.96 e^- per *f.u.* for L11MNOF). Such discrepancies typically indicate the presence of oxygen redox during the Li intercalation/deintercalation process, which frequently occurs in Li-rich cathode materials.[9,11,18,32,33]

To characterize the contribution of oxygen redox to the capacity, we performed high-efficiency mRIXS at the O K-edge, which is used to detect oxidized lattice oxygen in a myriad of cathode materials.[11,32–34] Specifically, a fingerprint feature of oxidized oxygen typically appears at an emission energy of ≈524 eV and excitation energy of ~531 eV of the 2D RIXS map.[11,32–34] Indeed, the characteristic oxidized oxygen feature is clearly present at the 5-V-charged states for all three samples while absent in their pristine and discharged states (Figure 3F and Figure S6, Supporting Information), confirming the existence of reversible oxygen redox that can lead to the capacity enhancement. When oxygen oxidation occurs during electrochemical cycling, irreversible oxygen processes can potentially occur, typically leading to O_2 release.[9–11,32] Here, we performed differential electrochemical mass spectrometry (DEMS) measurements on all three samples to characterize the in situ O_2 and CO_2 evolution during the first electrochemical cycle (Figure S7,

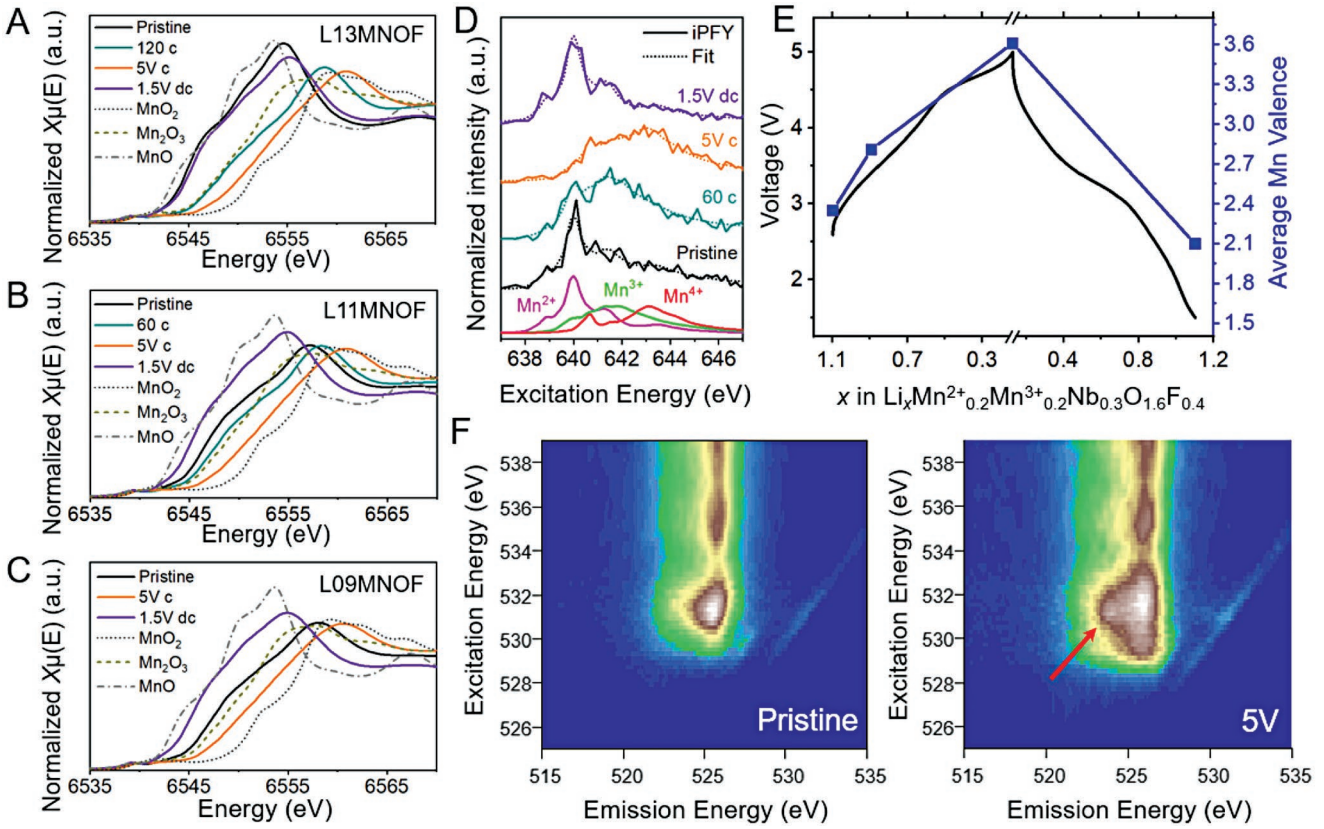

Figure 3. Mn K-edge XANES spectra of A) L13MNOF, B) L11MNOF, and C) L09MNOF at different states in the first cycle. D) Ex situ Mn L_3-edge mRIXS-iPFY spectra of L11MNOF at different states in the first cycle. Standard spectra of Mn^{2+}, Mn^{3+}, and Mn^{4+} are included at the bottom as references. E) Quantified Mn valence (blue squares) from mRIXS-iPFY overlaid on the first-cycle voltage profile (black curve). F) O K-edge RIXS maps of L11MNOF in the pristine and 5-V-charged states. The red arrow marks the oxidized oxygen feature.

Supporting Information). Presumably due to a high level (20%) of fluorination, all three samples showed negligible oxygen release (<0.01 μmol mg^{-1}) even after being charged to 5 V. As noted in previous studies,[8,35–37] the majority of detected O_2 originates from the irreversible oxygen redox near the cathode surface, which leaves behind a TM-densified surface layer and impedes Li transport. A similar level of oxygen loss within these samples is consistent with their nearly identical capacity loss over extended cycling (19.4% for L13MNOF, 21.2% for L11MNOF, and 19.9% for L09MNOF within 25 cycles) (Figure 2 and Figure S8, Supporting Information). Additionally, there is a noticeable amount of CO_2 evolved from these samples (0.31 μmol mg^{-1} for L13MNOF, 0.13 μmol mg^{-1} for L11MNOF, and 0.12 μmol mg^{-1} for L09MNOF), which likely originates from both decomposition of surface carbonate species (e.g., Li_2CO_3 formed during mixing carbon with active materials) and electrolyte decomposition.[9,37]

3. Computational Analysis of Cation SRO of Li-Mn-Nb-O-F Compounds

As discussed earlier in this paper, Mn^{2+}-Nb^{5+}-based DRX systems exhibit SRO that leads to less favorable Li-percolation than their Mn^{3+}-Nb^{5+}-based counterparts.[13,18,38] Our argument put forward is that synthesizing Mn^{3+}-Nb^{5+}-based DRX in a partially delithiated state could allow utilization of Mn^{2+}/Mn^{3+} redox while maintaining the superior SRO from Mn^{3+}. To achieve a more quantitative understanding of the percolation properties of L13MNOF, L11MNOF, and L09MNOF, we implemented ab-initio cluster-expansion Monte Carlo (CEMC) to investigate their SRO and percolating Li content.[13,16] The cluster-expansion Hamiltonian was fitted with DFT calculations in the chemical space of Li^{+}-$Mn^{2+/3+}$-Nb^{5+}-Vac-O^{2-}-F^{-} (see Methods). We simulated the atomic ordering of the as-synthesized compounds with different concentrations of cation vacancies ($Li_{1.3/1.1/0.9}Mn_{0.4}Nb_{0.3}O_{1.6}F_{0.4}$) by using canonical CEMC at $T = 2023$ K. This simulation temperature was calibrated for the ball-milling synthesis condition from the previously reported Li–Mn–O–F DRX system.[15] Overall, 1000 simulated structures were sampled from the Monte Carlo equilibrium ensemble, and the SRO was averaged over these sampled structures. For percolation purposes, lithium and vacancies were considered equivalent since the latter can be occupied by Li in the discharge.

As shown in **Figure 4**A, the amount of Li sites that are part of the percolating clusters increases in the order of L13MNOF (75%) < L11MNOF (80%) < L09MNOF (87%), confirming that the presence of cation vacancies and Mn^{3+} in the synthesis of L11MNOF and L09MNOF improves their SRO and thus Li

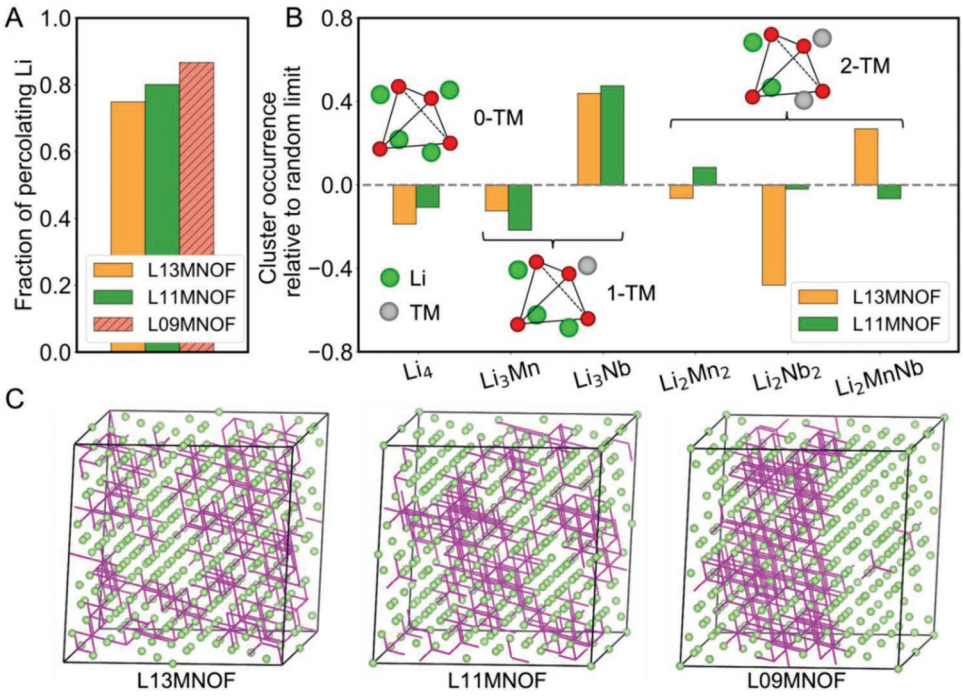

Figure 4. A) Fraction of percolating Li content in L13MNOF (orange), L11MNOF (green), and L09MNOF (red dashed). The dashed bar indicates that the state of L09MNOF is nondisordered at the simulation temperature $T = 2023$ K. B) Occurrence of various tetrahedral clusters (0-TM, 1-TM, and 2-TM) in cation-disordered L13MNOF (orange) and L11MNOF (green) as compared to the random limit. C) An illustration of simulated structures for L13MNOF, L11MNOF, and L09MNOF. The green ball represents the Li atom, and the magenta line represents the distribution of the bond between Mn and its nearest anion.

diffusion kinetics. We note that for L09MNOF the simulation temperature ($T = 2023$ K) and composition put the system in a part of the phase diagram where phase separation is occurring (Figure 4C and Figure S9, Supporting Information). Therefore, even though a higher percolating Li content is predicted for L09MNOF in the Monte Carlo simulation, the increased percolating Li content comes from the Li-rich phase, rather than from the desirable disordered phase. This result also indicates that the concentration of cation vacancies that can be achieved in high-temperature synthesis is limited. The phase behavior of these simulated compounds is consistent with the experimental observation, as L13MNOF and L11MNOF can be synthesized as single-phase DRX compounds while an obvious impurity phase exists in the as-synthesized L09MNOF (Figure 1A).

The SRO within L13MNOF and L11MNOF was further evaluated by comparing the occurrence (f_{calc}) of different tetrahedral clusters (0/1/2-TM channels) with respect to their frequency (f_{rand}) in random limit $(f_{calc} - f_{rand})/f_{rand}$ (Figure 4B). As mentioned above, the cation SRO in DRX systems was found to be affected by two major factors: the local charge balance and the ionic radius of the cations.[13,18] These insights can be used to rationalize the effect of cation vacancies. Because the cation vacancy has lower charge than the Li-ion, there is a higher tendency for a cation vacancy to mix with a high-valent cation (Nb^{5+}) so as to maintain local charge balance. For example, assuming all four anions (Figure 4B inset) on a tetrahedron to be O^{2-}, the average charge of the anions is -2. The cluster Li_2Nb_2 has an average charge of $(1 \times 2 + 5 \times 2)/4 = +3$, which is highly charge unbalanced. Therefore, its occurrence should be minimal in L13MNOF (the lowest orange bar of L13MNOF in Figure 4B). However, the average charge of the Vac_2Nb_2 cluster is $(0 \times 2 + 5 \times 2)/4 = +2.5$, which is closer to the charge balance than L13MNOF. As a result, the Vac_2Nb_2 forms with higher frequency than Li_2Nb_2. The size effect of a vacancy versus a Li-ion is more difficult to gauge, but their incorporation will induce distortion and strain to neighbor sites. In DRX compounds, the energy penalty to accommodate such lattice distortion is significantly lower for d^0 TM cations[37] (e.g., Nb^{5+}) than for those with partially filled d-orbitals (e.g., d^5 for Mn^{2+} and d^4 for Mn^{3+}). On this basis one would also expect the Vac_2Nb_2 cluster formation to be energetically more favored than the Li_2Nb_2 one. Taken together, both local charge balance and lattice distortion promote the formation of Vac-Nb clusters. On the other hand, due to the larger lattice mismatch of Li with Mn^{3+} than with Mn^{2+}, there is a higher tendency for Mn^{3+} to segregate from Li, which increases 0-TM channels and decreases Mn-containing 1-TM and 2-TM channels: the total occurrence of Mn-containing 2-TM (Li_2Mn_2 and Li_2MnNb) and 1-TM (Li_3Mn) channels is lower in L11MnOF (42%) than L13MnOF (48%) (Figure 4B). Indeed, such Vac-Nb gathering and Li-Mn separation become even more significant in the CEMC-simulated L09MNOF compound, where the compound decomposes into (1) Li-Vac-Nb-rich and (2) Mn-rich regions with a majority of Nb atoms (≈80%) and vacancies (≈95%) located in the region (1). Although region (1) has excellent Li percolation, it lacks in Mn redox and is not useful as a cathode material, which may explain why the impure L09MNOF compound performs slightly worse than L11MNOF. Therefore, to

fully utilize the superior SRO enabled by cation vacancies while keeping sufficient TM redox, a single-phase disordered structure must be maintained, which in turn requires that an appropriate amount of cation vacancies be introduced (e.g., 10% of vacancies in L11MNOF).

4. Conclusion

In summary, we successfully incorporated predesigned amounts of cation vacancies into the disordered rock salt structure of $Li_{1.3}Mn^{2+}_{0.4}Nb_{0.3}O_{1.6}F_{0.4}$ by synthesizing the compound at a partially charged state. Using a combination of ab initio and spectroscopic tools, we confirm that this partial Li deficiency strategy results in both Mn^{2+}/Mn^{3+} redox and excellent Li percolation due to the presence of Mn^{3+}, therefore delivering increased discharge capacity and rate performance. The vacancy concentration needs to be appropriately controlled as extensive vacancy doping (e.g., 20% vacancies in $Li_{0.9}Mn^{3+}_{0.4}Nb_{0.3}O_{1.6}F_{0.4}$) creates phase separation between a Li-Nb-rich phase and Mn-rich phase, which impairs the cathode performance. Taken together, this work extends the DRX design space to nonstoichiometric compounds, providing additional opportunities to optimize their performance.

5. Experimental Section

Synthesis: All the Li–Mn–Nb–O–F compounds were synthesized using mechanochemical ball milling. Li_2O (Alfa Aesar, ACS, 99% min), MnO (Sigma-Aldrich, 99.99%), Mn_2O_3 (Alfa Aesar, 99%), Nb_2O_5 (Alfa Aesar, 99.9%), and LiF (Alfa Aesar, 99.99%) were used as precursors. Stoichiometric amounts of the precursors were dispersed into Ar-filled stainless-steel jars and then planetary ball-milled (Retch PM 200) at a rate of 450 rpm for 45 h. In each jar, the total amount of precursors was ≈1 g. Five 10-mm (diameter) and ten 5-mm-(diameter) stainless balls were used as the grinding media.

Electrochemistry: The cathode film was prepared by mixing the active material, carbon black (Timcal, SUPER C65), and polytetrafluoroethylene (PTFE, DuPont, Teflon 8A) at a weight ratio of 70:20:10. Specifically, 280 mg of active materials and 80 mg of carbon black were mixed and shaker-milled for 1 h in an argon atmosphere using a SPEX 800 M Mixer/Mill. PTFE was then added and manually mixed with the shaker-milled mixture for 30 min. The components were then rolled into a thin film inside an Ar-filled glove box. The coin cell was assembled using the cathode film, a glass microfiber filter (Whatman), Li-metal foil (FMC), and electrolyte in an Ar-filled glove box and was tested on an Arbin battery test instrument at room temperature. The electrolyte used was 1 M $LiPF_6$ in a 1:1 (volume ratio) mixture of ethylene carbonate and dimethyl carbonate (BASF). The loading density of active material was ≈3 mg cm^{-2} for each cathode film, and the specific capacity was calculated based on the amount of the active compounds in the cathode film. The GITT measurement was performed by charging/discharging the coin cell for 30 min at a current density of 20 mA g^{-1}, followed by relaxing for 6 h to reach a quasi-equilibrium state. The electrochemically delithiated/lithiated samples were prepared by charging/discharging the assembled cells to predesigned states at a current density of 20 mA g^{-1}, followed by disassembling the cell and washing the cathode films with diethyl carbonate (DEC) in an Ar-filled glove box.

Characterization: XRD patterns of the as-prepared materials were collected using a Rigaku MiniFlex diffractometer (Cu source). Rietveld refinement was performed using the PANalytical X'Pert HighScore Plus software. SEM images were obtained using a Zeiss Gemini Ultra-55 analytical field-emission scanning electron microscope at the Molecular Foundry at Lawrence Berkeley National Laboratory (LBNL) with an acceleration voltage of 5 kV. STEM images and EDS elemental maps were collected using a FEI Titan X microscope equipped with a Bruker windowless EDS detector at an acceleration voltage of 300 kV. Elemental analysis was performed using a PerkinElmer Optima 5300 DV Optical Emission Spectrometer for lithium, manganese, and niobium. Fluorine content was determined using a pyrohydrolysis-based method at Galbraith Laboratories, Inc.

Hard X-Ray Absorption Spectroscopy: Mn and Nb K-edge XANES measurements were performed in transmission mode at beamline 20 BM at the Advanced Photon Source, Argonne National Laboratory. The incident beam energy was selected using a Si (111) monochromator, and the energy calibration was conducted by simultaneously measuring the spectra of the corresponding metal foil. Several reference standards spectra were also measured to aid the interpretation of the XANES data. The raw data were normalized and calibrated using Athena software.[39,40]

mRIXS: mRIXS data were collected at the iRIXS endstation at beamline 8.0.1 at the Advanced Light Source, Lawrence Berkeley National Laboratory. The samples were mounted on a copper sample holder and transferred into the main chamber using a sealed sample transfer kit from the Ar-filled glove box. The mRIXS data were collected using an ultrahigh-efficiency modular spectrometer with an excitation energy step of 0.2 eV. The resolution of the excitation and emission energy were 0.35 and 0.25 eV, respectively. Details of the experimental setups and the RIXS data processing have been described in previous reports.[41,42]

Mn-L_3 iPFY: As described in the previous publication,[43] Mn-L_3 iPFY spectra were obtained using the formula iPFY = a / PFY_O, where a is a normalization coefficient and PFY_O is the integrated fluorescence intensity over the O-K emission energy range (490–530 eV) from the Mn-L_3 mRIXS. The spectra were further quantitatively fitted using a linear combination of the standard spectra of $Mn^{2+/3+/4+}$.

Differential Electrochemical Mass Spectrometer Measurement: The custom-built DEMS instrument, cell geometry, and instrument operation are described in previous publications.[44,45] The electrochemical cells were prepared in a glove box using a modified Swagelok design and were cycled at 20 mA g^{-1} under a positive Ar pressure (≈1.2 bar) at room temperature after being appropriately attached to the DEMS instrument. The cathodes and anode used were identical to those used for the coin-cell tests in this study. In each DEMS cell, one sheet of polypropylene film (Celgard 2500) and one sheet of QM-A quartz microfiber filters (Whatman) were used as separators with 80 µL of 1 M LiPF6 (Gotion) in EC/DEC (Gotion, 1:1 in volume ratio) added as the electrolyte. The loading density of active material was ≈14 mg cm^{-2} for the cathode film.

DFT Calculations: All the DFT calculations were performed using the Vienna ab initio simulation package (VASP)[46] using the projector-augmented wave method,[47] a plane-wave basis set with an energy cutoff equal to 520 eV, and a reciprocal space discretization of 25 k-points per Å. All the calculations were converged to 10^{-6} eV in total energy for electronic loops and 0.02 eV $Å^{-1}$ in interatomic forces for ionic loops. We relied on the regularized strongly constrained and appropriately normed meta-GGA exchange-correlation functional (r^2SCAN),[48,49] which is believed to better capture cation-anion hybridization and Li-coordination[50,51] and would improve the accuracy of the energetics when cation vacancies are introduced into the rocksalt. r^2SCAN has better computational efficiency performance than the earlier version of SCAN.[52]

Cluster Expansion: The cluster-expansion (CE) technique is used to study the configurational thermodynamics of materials in which sites can be occupied by multiple cations and has been applied to study the Li-vacancy configuration in layered materials[52] and the cation SRO in DRX compounds.[38,53,54] The CE expands the energy of multicomponent disordered rocksalt materials as a sum of many-body configurational interactions:

$$E(\sigma) = J_0 + \sum_i J_i \sigma_i + \sum_{i,j} J_{ij} \sigma_i \sigma_j + \sum_{i,j,k} J_{ijk} \sigma_i \sigma_j \sigma_k + \cdots \quad (1)$$

where σ_i is the occupancy of different species (indicator basis site function) and J refers to the effective cluster interaction (ECI). For

the simulation of atomic orderings, a cluster-expansion Hamiltonian was generated in the chemical space of Li^{+}-Mn^{2+}-Mn^{3+}-Nb^{5+}-vacancy-O^{2-}-F^{-}, with pair interactions up to 7.1 Å, triplet interactions up to 4.0 Å, and quadruplet interactions up to 4.0 Å based on a primitive cell of the rocksalt structure with lattice parameter $a = 3$ Å. In total, 281 ECIs (including the constant term J_0) were defined, and the CE Hamiltonian was fitted with 1206 different structures. As the CE Hamiltonian was defined on a high-dimensional multicomponent system, the ECIs were fitted using the appropriate method to address the complexity-induced over-fitting.[55–57] The ECIs were determined with the optimal sparseness and cross-validation error (<7 meV per atom) with a $\ell_0\ell_2$-norm regularized regression.[58]

To simulate atomic orderings at equilibrium, we used canonical Monte Carlo simulation with the Metropolis–Hastings algorithm. Overall, 1000 representative structures (960 atoms per structure) were sampled from the equilibrium ensemble. The percolating Li content and the different types of tetrahedra clusters were analyzed in these representative structures using the dribble package.[7]

Supporting Information

Supporting Information is available from the Wiley Online Library or from the author.

Acknowledgements

L.H. and P.Z. contributed equally to this work. This work was supported by the Assistant Secretary for Energy Efficiency and Renewable Energy, Vehicle Technologies Office, under the Applied Battery Materials Program, of the US Department of Energy (DOE) under contract no. DE-AC02-05CH11231. Research at the Advanced Light Source was supported by the Director, Office of Science, Office of Basic Energy Sciences, of the US DOE under contract no. DE-AC02-05CH11231. Research at the Molecular Foundry was supported by the Office of Science, Office of Basic Energy Sciences, of the U.S. Department of Energy under Contract No. DE-AC02-05CH11231. T.-Y.H. was supported collectively by both the Ministry of Education in Taiwan and the UC Berkeley College of Chemistry through the Taiwan Fellowship Program. The computational work was supported with the computational resources provided by the Extreme Science and Engineering Discovery Environment (XSEDE), which was supported by National Science Foundation grant number ACI1053575; the National Energy Research Scientific Computing Center (NERSC), a U.S. DOE Office of Science User Facility located at Lawrence Berkeley National Laboratory under contract no. DE-AC02-05CH11231; and the Lawrencium computational cluster resource provided by the IT Division at the Lawrence Berkeley National Laboratory.

Conflict of Interest

The authors declare no conflict of interest.

Data Availability Statement

The data that support the findings of this study are available from the corresponding author upon reasonable request.

Keywords

cation vacancies, cation-disordered cathodes, Li-ion batteries, percolation properties, short-range order

Received: July 11, 2022
Revised: October 31, 2022
Published online:

[1] K. Kang, Y. S. Meng, J. Breger, C. P. Grey, G. Ceder, *Science* **2006**, *311*, 977.
[2] B. Xu, D. Qian, Z. Wang, Y. S. Meng, *Mater. Sci. Eng., R Rep.* **2012**, *73*, 51.
[3] N. Yabuuchi, *Chem. Rec.* **2019**, *19*, 690.
[4] J. B. Goodenough, Y. Kim, *Chem. Mater.* **2010**, *22*, 587.
[5] L. Xie, C. Singh, S. K. Mitter, M. A. Dahleh, S. S. Oren, *Joule* **2021**, *5*, 1908.
[6] E. A. Olivetti, G. Ceder, G. G. Gaustad, X. Fu, *Joule* **2017**, *1*, 229.
[7] A. Urban, J. Lee, G. Ceder, *Adv. Energy Mater.* **2014**, *4*, 1400478.
[8] J. Lee, J. K. Papp, R. J. Clément, S. Sallis, D.-H. Kwon, T. Shi, W. Yang, B. D. McCloskey, G. Ceder, *Nat. Commun.* **2017**, *8*, 981.
[9] J. Lee, D. A. Kitchaev, D.-H. Kwon, C.-W. Lee, J. K. Papp, Y.-S. Liu, Z. Lun, R. J. Clement, T. Shi, B. D. McCloskey, J. Guo, M. Balasubramanian, G. Ceder, *Nature* **2018**, *556*, 185.
[10] Z. Lun, B. Ouyang, Z. Cai, R. J. Clément, D.-H. Kwon, J. Huang, J. K. Papp, M. Balasubramanian, Y. Tian, B. D. McCloskey, H. Ji, H, K. , D. A. Kitchaev, G. Ceder, *Chem* **2020**, *6*, 153.
[11] Z. Lun, B. Ouyang, D.-H. Kwon, Y. Ha, E. E. Foley, T.-Y. Huang, Z. Cai, H. Kim, M. Balasubramanian, Y. Sun, J. Huang, Y. Tian, H. Kim, B. D. McCloskey, W. Yang, R. J. Clément, H. Ji, G. Ceder, *Nat. Mater.* **2021**, *20*, 214.
[12] J. Lee, A. Urban, X. Li, D. Su, G. Hautier, G. Ceder, *Science* **2014**, *343*, 519.
[13] H. Ji, A. Urban, D. A. Kitchaev, D.-H. Kwon, N. Artrith, C. Ophus, W. Huang, Z. Cai, T. Shi, J. C. Kim, H. Kim, G. Ceder, *Nat. Commun.* **2019**, *10*, 592.
[14] R. Chen, S. Ren, M. Knapp, D. Wang, R. Witter, M. Fichtner, H. Hahn, *Adv. Energy Mater.* **2015**, *5*, 1401814.
[15] D. A. Kitchaev, Z. Lun, W. D. Richards, H. Ji, R. J. Clément, M. Balasubramanian, D.-H. Kwon, K. Dai, J. K. Papp, T. Lei, B. D. McCloskey, W. Yang, J. Lee, G. Ceder, *Energy Environ. Sci.* **2018**, *11*, 2159.
[16] J. Huang, P. Zhong, Y. Ha, D.-H. Kwon, M. J. Crafton, Y. Tian, M. Balasubramanian, B. D. McCloskey, W. Yang, G. Ceder, *Nat. Energy* **2021**, *6*, 706.
[17] M. A. Jones, P. J. Reeves, I. D. Seymour, M. J. Cliffe, S. E. Dutton, C. P. Grey, *Chem. Commun.* **2019**, *55*, 9027.
[18] R. J. Clément, Z. Lun, G. Ceder, *Energy Environ. Sci.* **2020**, *13*, 345.
[19] H. Lee, W. Choi, W. Lee, J. Shim, Y. Kim, W. Yoon, *Adv. Energy Mater.* **2021**, *11*, 2002958.
[20] W. H. Kan, B. Deng, Y. Xu, A. K. Shukla, T. Bo, S. Zhang, J. Liu, P. Pianetta, B.-T. Wang, Y. Liu, G. Chen, *Chem* **2018**, *4*, 2108.
[21] R. Satish, L. Wichmann, M. J. Crafton, R. Giovine, L. Li, J. Ahn, Y. Yue, W. Tong, G. Chen, C. Wang, R. J. Clément, R. Kostecki, *ChemElectroChem* **2021**, *8*, 3982.
[22] A. Van der Ven, G. Ceder, *J. Power Sources* **2001**, *97*, 529.
[23] A. Van der Ven, J. Bhattacharya, A. A. Belak, *Acc. Chem. Res.* **2013**, *46*, 1216.
[24] Z. Cai, Y. Zhang, Z. Lun, B. Ouyang, L. C. Gallington, Y. Sun, H. Hau, Y. Chen, M. C. Scott, G. Ceder, *Adv. Energy Mater.* **2022**, *12*, 2103923.
[25] R. D. Shannon, *Acta Crystallogr., Sect. A Found. Adv.* **1976**, *32*, 751.
[26] K. Saravanan, P. Balaya, M. V. Reddy, B. V. R. Chowdari, J. J. Vittal, *Energy Environ. Sci.* **2010**, *3*, 457.
[27] D. Zhang, J. P. Tu, J. Y. Xiang, Y. Q. Qiao, X. H. Xia, X. L. Wang, C. D. Gu, *Electrochim. Acta* **2011**, *56*, 9980.
[28] H. Li, R. Fong, M. Woo, H. Ahmed, D.-H. Seo, R. Malik, J. Lee, *Joule* **2021**, *6*, 53.
[29] T. Sato, K. Sato, W. Zhao, Y. Kajiya, N. Yabuuchi, *J. Mater. Chem. A* **2018**, *6*, 13943.
[30] J. Lee, C. Wang, R. Malik, Y. Dong, Y. Huang, D. Seo, J. Li, *Adv. Energy Mater.* **2021**, *11*, 2100204.
[31] A. Manceau, M. A. Marcus, S. Grangeon, *Am. Mineral.* **2012**, *97*, 816.

[32] J. Wu, Z. Zhuo, X. Rong, K. Dai, Z. Lebens-Higgins, S. Sallis, F. Pan, L. F. J. Piper, G. Liu, Y. Chuang, Z. Hussain, Q. Li, R. Zeng, Z. Shen, W. Yang, *Sci. Adv.* **2020**, *6*, eaaw3871.
[33] K. Dai, J. Wu, Z. Zhuo, Q. Li, S. Sallis, J. Mao, G. Ai, C. Sun, Z. Li, W. E. Gent, *Joule* **2019**, *3*, 518.
[34] Z. Zhuo, K. Dai, R. Qiao, R. Wang, J. Wu, Y. Liu, J. Peng, L. Chen, F. Pan, Z. Shen, *Joule* **2021**, *5*, 975.
[35] L. Li, Z. Lun, D. Chen, Y. Yue, W. Tong, G. Chen, G. Ceder, C. Wang, *Adv. Funct. Mater.* **2021**, *31*, 2101888.
[36] J. Lee, D.-H. Seo, M. Balasubramanian, N. Twu, X. Li, G. Ceder, *Energy Environ. Sci.* **2015**, *8*, 3255.
[37] T.-Y. Huang, M. J. Crafton, Y. Yue, W. Tong, B. D. McCloskey, *Energy Environ. Sci.* **2021**, *14*, 1553.
[38] B. Ouyang, N. Artrith, Z. Lun, Z. Jadidi, D. A. Kitchaev, H. Ji, A. Urban, G. Ceder, *Adv. Energy Mater.* **2020**, *10*, 1903240.
[39] B. Ravel, M. Newville, *J Synchrotron Radiat* **2005**, *12*, 537.
[40] B. Ravel, M. Newville, *Phys. Scr.* **2005**, *2005*, 1007.
[41] R. Qiao, Q. Li, Z. Zhuo, S. Sallis, O. Fuchs, M. Blum, L. Weinhardt, C. Heske, J. Pepper, M. Jones, A. Brown, A. Spucces, K. Chow, B. Smith, P. A. Glans, Y. Chen, S. Yan, F. Pan, L. F. J. Piper, J. Denlinger, J. Guo, Z. Hussain, Y. Chuang, W. Yang, *Rev. Sci. Instrum.* **2017**, *88*, 033106.
[42] J. Wu, S. Sallis, R. Qiao, Q. Li, Z. Zhuo, K. Dai, Z. Guo, W. Yang, *J Vis Exp* **2018**, *134*, e57415.
[43] Q. Li, R. Qiao, L. A. Wray, J. Chen, Z. Zhuo, Y. Chen, S. Yan, F. Pan, Z. Hussain, W. Yang, *J Phys D Appl Phys* **2016**, *49*, 413003.
[44] B. D. McCloskey, D. S. Bethune, R. M. Shelby, G. Girishkumar, A. C. Luntz, *J. Phys. Chem. Lett.* **2011**, *2*, 1161.
[45] B. D. McCloskey, A. Speidel, R. Scheffler, D. C. Miller, V. Viswanathan, J. S. Hummelshøj, J. K. Nørskov, A. C. Luntz, *J. Phys. Chem. Lett.* **2012**, *3*, 997.
[46] G. Kresse, D. Joubert, *Phys. Rev. B* **1999**, *59*, 1758.
[47] G. Kresse, J. Furthmüller, *Comput. Mater. Sci.* **1996**, *6*, 15.
[48] J. W. Furness, A. D. Kaplan, J. Ning, J. P. Perdew, J. Sun, *J. Phys. Chem. Lett.* **2020**, *11*, 8208.
[49] J. Sun, A. Ruzsinszky, J. P. Perdew, *Phys. Rev. Lett.* **2015**, *115*, 36402.
[50] Y. Zhang, D. A. Kitchaev, J. Yang, T. Chen, S. T. Dacek, R. A. Sarmiento-Pérez, M. A. L. Marques, H. Peng, G. Ceder, J. P. Perdew, J. Sun, *NPJ Comput. Mater.* **2018**, *4*, 9.
[51] J. H. Yang, D. A. Kitchaev, G. Ceder, *Phys. Rev. B* **2019**, *100*, 35132.
[52] R. Kingsbury, A. S. Gupta, C. J. Bartel, J. M. Munro, S. Dwaraknath, M. Horton, K. A. Persson, *Phys. Rev. Mater.* **2022**, *6*, 13801.
[53] P. Zhong, Z. Cai, Y. Zhang, R. Giovine, B. Ouyang, G. Zeng, Y. Chen, R. Clément, Z. Lun, G. Ceder, *Chem. Mater.* **2020**, *32*, 10728.
[54] R. J. Clément, D. Kitchaev, J. Lee, G. Ceder, *Chem. Mater.* **2018**, *30*, 6945.
[55] L. J. Nelson, G. L. W. Hart, F. Zhou, V. Ozoliņš, *Phys. Rev. B* **2013**, *87*, 35125.
[56] A. Seko, A. Takahashi, I. Tanaka, *Phys. Rev. B* **2014**, *90*, 24101.
[57] Z. Leong, T. L. Tan, *Phys. Rev. B* **2019**, *100*, 134108.
[58] P. Zhong, T. Chen, L. Barroso-Luque, F. Xie, G. Ceder, *Phys. Rev. B* **2022**, *106*, 024203.